Generation of a Fibrillar Core in PET Fiber by Cold Drawing

O. R. HUGHES, D. K. KURSCHUS, C. K. SAW, J. FLINT, T. P. BRUNO, R. T. CHEN

Hoechst Corporate Research & Technology Center, Summit, New Jersey 07901

Received 12 June 1998; accepted 14 January 1999

ABSTRACT: Cold draw processing of poly(ethylene terephthalate) yarns has been discovered that yields a sheath/fibrillar core (s/fc) microstructure in the each fiber of a yarn. When aged, unoriented, noncrystalline spun yarns were cold drawn, high (>5.7 : 1) draw ratios could be achieved and an s/fc microstructure resulted. Cold drawing also generated a high oriented amorphous content. The tensile and shrinkage properties of yarns with the s/fc microstructure and high oriented amorphous content were examined as function of processing (drawing, annealing, and relaxing). The microstructure was examined by scanning electron microscopy, transmission electron microscopy, small-angle X-ray scattering, wide-angle X-ray scattering, and optical microscopy. The fibrillar microstructure survives all processing. Management of the oriented amorphous component under heat and tension contributes to the greater stiffness (modulus) and dimensional stability of processed s/fc yarns. The properties of yarns with an s/fc microstructure are compared with more conventional hot drawn yarns. © 1999 John Wiley & Sons, Inc. J Appl Polym Sci 74: 2335–2352, 1999

Key words: fiber drawing; cold drawing; fiber microstructure; fiber properties; poly(ethylene terepthalate)

INTRODUCTION

Poly(ethylene terephthalate) (PET) yarns have been highly developed for reinforcing applications, most notably as tire cords in radial-ply tire rubber reinforcement. The most successful PET product, the so-called high modulus, low shrink (HMLS) yarns, are valued for their tensile strength, stiffness (initial tensile modulus), and dimensional stability,[1,2] as well as low cost and availability. The properties of HMLS fibers are based on a polymer microstructure that has several components. Prevorsek and colleagues[3–5] described these as polymers in crystalline, disordered domain, and extended-chain, noncrystalline forms. Similar components are referred to in discussions of X-ray spectra as crystalline, unoriented amorphous (UOA) and oriented amorphous (OA) components. In the Prevorsek model, crystallites and disordered domains lie in series to form microfibrils. The extended-chain, noncrystalline molecules lie in parallel strands between the microfibrils but are a small proportion of the total.

It is possible to achieve higher fiber stiffness through high-stress processing. The objective is to achieve a greater fraction of polymer chains that are extended and aligned with the fiber axis. When this is achieved it is often at the cost of a loss in stabilizing crystallinity. Such fibers usually exhibit greater shrinkages when warmed and are thus considered to lack dimensional stability.

Kunugi[6–11] and Suzuki and colleagues[12–15] have shown that high stiffnesses can be developed in PET fibers if unoriented, noncrystalline fibers

Correspondence to: O. R. Hughes, 31 Dogwood Drive, Chatham, NJ 07928 (orh@aol.com).

Journal of Applied Polymer Science, Vol. 74, 2335–2352 (1999)
 CCC 0021-8995/99/102335-18

are zone drawn, incrementally in multiple stages, to high draw ratios and zone annealed. Their intent in continuous zone drawing (CZD) is to slowly extend and align the polymer while generating as little crystallinity as possible. CZA is then applied to increase crystallinity. The CZA fibers exhibited high tensile strength (1.2 GPa) and modulus (16 GPa), but shrinkage of these fibers was not discussed.

Cuculo and colleagues[16] formed PET fibers via high-speed spinning through a stress-enhancing liquid isothermal bath (LIB). These fibers exhibit high strength, stiffness, and dimensional stability. It was suggested that they contain a taut-tie noncrystalline (TTNC) phase. This appears to be the same component as the extended chain or OA component, referred to here. The TTNC phase is present along with crystallites and a random amorphous phase. The TTNC content in a variety of LIB fibers ranged from 8 to 14%, whereas conventional and HMLS yarns were estimated to have from 2 to 8% and 6 to 10% TTNC, respectively. The initial modulus of fibers was directly proportional to the TTNC content reaching 150 g/denier at 14% TTNC content. The hot air shrinkages of drawn and annealed LIB fibers were in the range of 5–6%. This compares with hot air shrinkages of 6% for HMLS and about 14% for conventional tire cord.

The property of necking during cold drawing was described by Marshall and Thompson.[17] Many polymers do not extend under tension like a rubber band. Instead, after an initial linear extension in response to applied tension, they neck down to a smaller cross section at specific point on the draw line and extend with no increase in applied tension until all the material has necked down. Then, further extension is possible with increasing applied tension until the breaking tenacity is exceeded.

The effects of preorientation and crystallinity in PET fibers on the draw ratios achieved on cold drawing was studied by Allison and Ward.[18,19] Preorientation produced marked changes in the draw ratio that could be achieved. A relatively small amount of preorientation, indicated by birefringence, sharply decreases the achievable draw ratio. A total birefringence of about 0.200 may be introduced into PET by large extensions; however, orientation as little as represented by a birefringence of 0.010 can significantly reduce the natural draw ratio.

S/fc microstructures have been noted in PET fibers, albeit infrequently, since their introduction.[20] Cobbold and colleagues[21] described fibrils with diameters in the 200–1000 Å range in 0.25 mm fibers but did not describe the processing that produced them. It was suggested[3] that the microfibrils thought to be present in the current HMLS-type PET fibers could be seen in transmission electron microscopy (TEM) images where they are estimated to have a diameter of approximately 80 Å.

Fibril-like microstructures have resulted from cold draw processing. Geil and colleagues[22–24] observed 75-Å-diameter nodular structures with paracrystalline-type order in glassy amorphous PET. Movement of the nodules was seen at annealing temperatures below T_g that leads to alignment of the nodules into fibrillar ribbons that crystallize as spherulites.

PET fiber spinners often refer to an effect that aging has on drawability of a spun fiber. The usual inference is that aged fiber, versus freshly spun fiber, cannot be extended to the same degree by hot drawing. In considering whether cold drawing would be similarly affected, our attention was drawn to an endotherm near the T_g in differential scanning calorimetry (DSC) scans of PET as a property that reflects aging history. Wunderlich and colleagues[25] studied the time-dependent apparent heat capacities of a variety of polymers, and Menczel[26] studied PET. They attributed the endotherm to configurational rearrangements that are frozen in at sub-T_g temperatures. More recently, Montsarrat and colleagues,[27,28] Wang and Shen,[29] and Qian and colleagues[30–32] have reexamined this phenomenon. Qian attributes the endotherm to heat needed to disrupt cohesive entanglements that are the result of local nematic interactions between neighboring chain segments in the condensed state. We suspected that this structure, produced by aging, might effect the outcome of cold drawing.

In the current work we have cold drawn sub-T_g aged, unoriented, noncrystalline PET yarns under conditions that a neck formed and high draw ratios were achieved. Surprisingly, each fiber in the yarns had an s/fc microstructure that can be seen at 1000× magnification. Here, processing that generates this microstructure is explored, and the properties of fibers and yarns that have the structure are examined and compared to hot drawn PET fibers.

Table I Spun Yarn Properties

Yarn	Spin Speed (mpm)	Denier (57 fil/pkg)	Den./Fil.	Bi	η_{inh} (dL/g)
S1	200	2031	36	0.001	0.63
S2	2000	375	6.6	0.030	0.75
S3	4000	255	4.5	0.084	0.75

EXPERIMENTAL

Resins

A high molecular weight polymer without additives was made by melt polymerization without need for solid state processing. The resin was extruded from the reactor as an $\frac{1}{8}''$ diameter strand and chopped. The resins used for (1) 200 mpm spinning and (2) for 2000 and 4000 mpm spinning had inherent solution viscosities, η_{inh} of 0.80 and 0.93 dL/g in *o*-chlorophenol at 25°C, respectively. The carboxyl end group content was 23 μeq/g, and the diethylene glycol content was approximately 1 wt %.

Spinning

The $\frac{1}{8}''$ extrudate was dried (130°C, vac, 2 days) prior to spinning and transferred to the spinning column hopper without contact with ambient atmosphere. Nineteen filament yarns S1, S2, and S3 were melt extruded at 300°C at speeds of 200, 2000, and 4000 mpm with the results in Table I. An aqueous spin finish was applied prior to take up. Melt extrusion caused a small declines in molecular weight. The carboxyl end group content was 45 μeq/g, and the diethylene glycol content was approximately 1.1 wt %. Yarns (57 filaments) for drawing were formed by combining three packages of the 19 filament spun yarns.

Aging

A yarn S1a was prepared from S1 for cold drawing by aging at 65°C for 144 h while the yarn was wrapped on bobbins. This generates an endotherm in the DSC heating scan of S1a, at temperatures near the T_g, as shown in Figure 1. It was found empirically that only aged yarns, such as S1a, having this endotherm yield a uniform s/fc microstructure when cold drawn.

Cold Drawing

The single stage draw frame in Figure 2 was used for cold drawing S1a to yield II, a yarn whose fibers each had an s/fc microstructure. The parameters are listed in Table II. A cold neck was a necessary but not sufficient condition for the formation of the s/fc microstructure. The neck was initiated by heating the moving yarn under tension. For this purpose the draw line was equipped with a 14-cm tube oven that was heated by a flow of controlled-temperature N_2 gas. The neck was initiated in S1a by hot (100°C) N_2 gas flowing through the tube with a load of 650 g on the yarn. Once initiated, the neck could be maintained with little or no heat. The neck localized at a position 2 to 4″ before the (upstream from) tube where the temperature was close to ambient. The necks in all fibers of the yarn bundle occurred together at the same location on the draw line. This appears to be a "coupling" of necks.[17] The length of the neck bundle was approximately 1 mm. The ratio of deniers (S1a : II) was 6.0 : 1, indicating a draw ratio, λ, of 6.0 : 1. Frequent fiber breakage occurred when higher line loads were attempted. Attaining draw ratios higher than 5.7 : 1 through cold drawing was enabled by aging. Draw ratios greater than 5.7 : 1 could not be achieved with S1, and an s/fc microstructure could not be uniformly generated in S1.

Annealing and Relaxing

The single stage unit in Figure 2 was used for annealing (II $\Rightarrow$ III) and relaxing (III $\Rightarrow$ IV and II $\Rightarrow$ V) yarns. For this purpose it was equipped with a 1-m electric oven. The process conditions are tabulated in Table II.

Multistage Hot Drawings

When S1, S2, and S3 were hot drawn by a multistep process using the more conventional, three-stage, draw frame equipped with hot shoes in Figure 2, D1, D2, and D3 resulted. The conditions are tabulated in Table III.

Heat Treating

To simulate the conditions that a tire yarn is exposed to during conversion to tire cord and tire

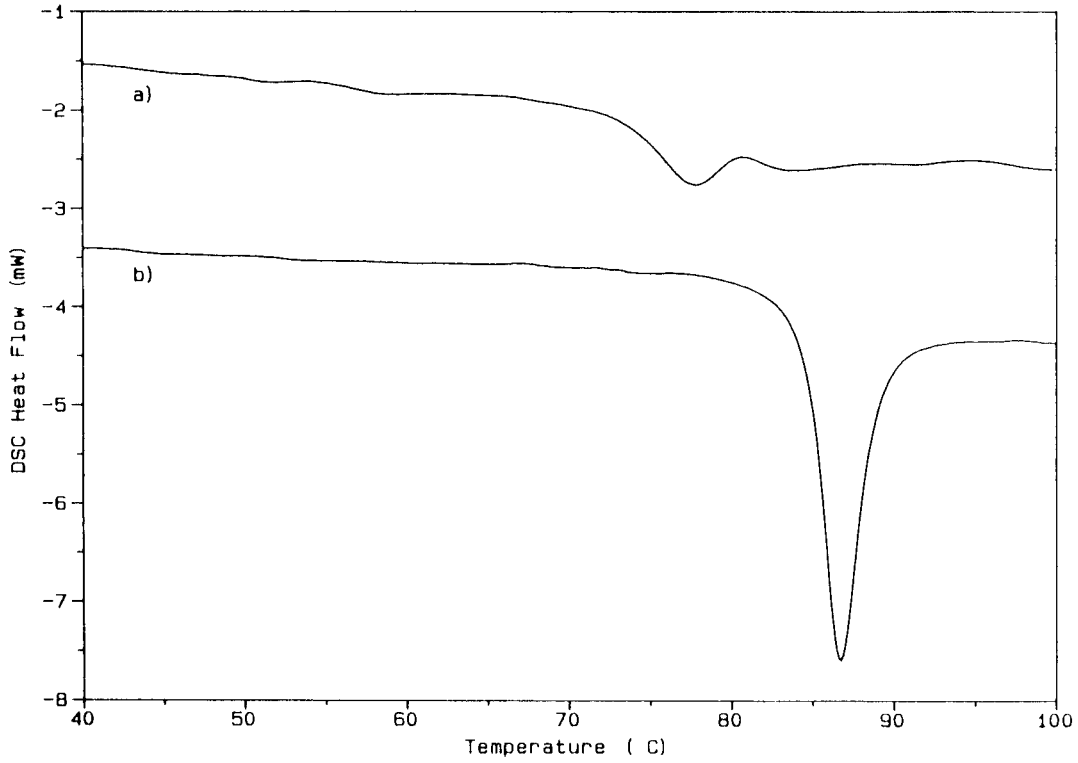

Figure 1 Effect of aging on DSC thermograms: 40–100°C: a) S1, before annealing; b) S1a, after annealing for 144 h at 65°C.

building, the high speed yarns D2 and D3 were heat treated on the draw frame in Figure 2 equipped with 1 m and 2 m ovens. The heat treatment was done under a variety of conditions (temperatures of 180–240°C, loads of 0.2–1.0 g/den, residence times of 10–60 s). This led to a family of heat treated yarns HT, the best performing of which fell in the area designated HT in Figure 11 (see below). The heat treatment did not include the application of a resorcinol formaldehyde latex (RFL) adhesion promoting coating.

Tensile Properties

Tensile properties of yarn samples (10″ gage length) were measured on an Instron Universal Tester at a crosshead speed of 6″/min to achieve a rate of 60%/min according to ASTM 03.01 D885-79. Yarns were conditioned for 24 h at 65% RH and 70°F prior to testing. Five yarn specimens from each sample were tested to break and the properties averaged.

EASL

The *e*longation that a yarn undergoes when subjected to *a s*pecified *l*oad (EASL) is a measure of fiber stiffness at practical applied stresses and hence a measure of yarn stiffness (stiffer yarn: lower EASL). EASL, as used here, is the percent increase in length of a 12″ length of yarn at 25°C under a load of 2 g/denier.

$$\text{EASL} = (l_f - l_i) \times 100/l_i \quad (1)$$

where l_i is the initial length and l_f is the final length.

Shrinkage

The hot air shrinkage (HAS) of 25 cm yarn specimens was measured after exposure in a hot air oven for 30 min at 177°C under a load of 0.1 g/denier. Shrinkage was calculated from the initial and final lengths (l_i, l_f) using the following equation:

$$\text{HAS}\ (\%) = (l_i - l_f) \times 100/l_i \quad (2)$$

Dimensional Stability

Dimensional stability refers to the ability of a fiber to retain its strength and stiffness as well as

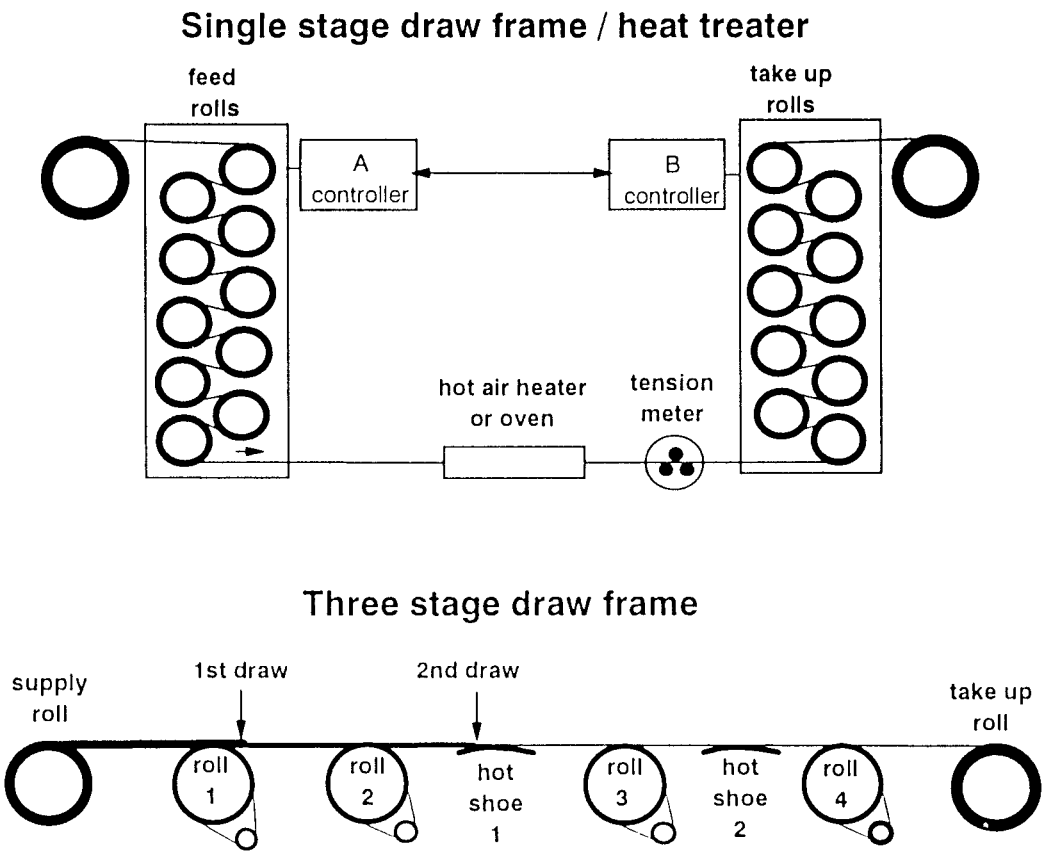

Figure 2 Draw frames.

its length dimension (shrink resistance) during manufacturing and use. A dimensionally stable yarn exhibits high stiffness and low shrinkage. In tire reinforcement, a yarn should retain its stiffness (high initial modulus or low EASL) and resist shrinking at the temperatures and tensions that are applied during (1) heat treating to convert yarn to cord, (2) tire building and curing, and (3) use. Yarns that have been drawn extensively are likely to be stiff but exhibit high HAS when subsequently heated unless stabilized in some manner. Relaxation during processing lowers

Table II Process Conditions for Cold Drawing, Annealing, and Relaxing

		Feed Rolls (m/min)	Take-up Rolls (m/min)	Load (g)	Oven Temp. (°C)	Draw Ratio[a] (λ)	Product Denier	Total Draw[b] (λ_t)	Density (g/cc)
Sequence: S1a ⇒ II ⇒ III ⇒ IV									
As spun	S1a						2031		1.340
Drawn	II	2.0	12.0	650	see text	6.0	333	6.1	< 1.310
Annealed	III	2.0	2.53	920	200	1.27	276	7.4	1.330
Relaxed	IV	2.0	1.88	45	200	0.94	311	6.5	1.355
Sequence: S1a ⇒ II ⇒ V									
Relaxed without annealing	V	2.0	1.64	20	200	0.82	410	5.0	1.313

[a] Calculated from ratio of initial to final denier.
[b] Observed as ratio of take-up roll speed to feed roll speed.

Table III Three-Stage, Hot Draw Conditions

Yarn	Speed at Roll 1 (mpm)	Shoe 1 Temp. (°C)	Speed at Roll 2 (mpm)	Shoe 2 Temp. (°C)	Speed at Roll 3 (mpm)	Shoe 3 Temp. (°C)	Speed at Roll 4 (mpm)	Product Denier (g)	Total Draw Ratio
D1	3.0	85	11.5	160	16.2	220	15.9	124	5.3
D2	10.0	25	11.0	160	24.4	220	24.0	50.0	2.5
D3	10.0	25	12.4	160	14.5	220	14.3	63.4	1.3

shrinkage but also lowers stiffness. We have used the sum of EASL plus HAS properties as a simple index of dimensional stability. The lower the index, the greater the dimensional stability.

Thermal

DSC thermograms were obtained on a TA Instruments system (controller model 2000, cell model 910) equipped with liquid N_2 cooling. The scan rate was 10°C/min except as noted. The temperature and heat scales were calibrated with an Indium reference sample. Yarn samples (typically 10 mg) were tautly wound on a jig to prevent shrinkage during the taut fiber DSC scans. This holds the fiber at constant length during the DSC scan and prevents relaxation and recrystallization that otherwise occur. Each scan began with a heating scan from ambient to 300°C and ended with a cooling scan from 300°C to ambient. Thermal transition temperatures and heats (glass transition, T_g; cold crystallization exotherm, T_{cc}, ΔH_{cc}; crystalline melting endotherm, T_m, ΔH_m) were extracted.[33] The degree of PET crystallinity, $\%n$, was determined by the ratio of the heats of cold crystallization and melting to the heat of melting of crystalline PET:

$$\%n = (\Delta H_m - \Delta H_{cc}) \times 100/\Delta H_{\text{crystalline PET}} \quad (3)$$

where $\Delta H_{\text{crystalline PET}} = 140$ J/g,[34]

Density

The densities of yarn samples were determined by observing the float level of a 2-in. length of yarn in a gradient column of $Ca(NO_3)_2$ in water, following ASTM 1505. The 100-cm column had a density gradient from 1.30 to 1.43 g/cc and was calibrated using graded density balloons (American Density Materials, Belvidere, MD).

SEM

In order to expose the core of fibers for scanning electron microscopy (SEM) examination, longitudinal cross-sectional surfaces were prepared by slicing the fibers longitudinally with a scalpel and peeling back the fiber surface. The specimen was then coated with a 50-Å Pt deposit by sputtering. The SEM imaging was conducted on a JEOL JXA-840 SEM operating at 5 kV.

TEM

For TEM study, the fiber samples were embedded in epoxy and thin sectioned (ca. 100 nm thick) using a Reichert ultramicrotome. Both transverse cross sections (perpendicular to the fiber axis) and near longitudinal cross sections (ca. 10° to the fiber axis) were prepared. The ultrathin sections were then coated with evaporated carbon and examined in a JEOL 100CX TEM operating at 100 kV.

OM (Polarized Light Optical Microscopy)

A Leitz Othoplan polarized light microscope was used to examine the fibers in an immersion oil through two perpendicularly-oriented polarizing filters.

Birefringence

The birefringence of fiber samples immersed in a refractive index oil was measured using a Leitz polarized light microscope equipped with Berek tilt-type compensators with varying orders of retardation. Five different fiber specimens from each yarn were measured and averaged.

WAXS

Two-dimensional wide-angle X-ray scattering (WAXS) measurements were carried out using a modified Philips vertical goniometer adapted to

rotate the fiber in the direction perpendicular to the scattering plane. An analyzing graphite monochromator was used on the diffracted beam. The experiment was performed in transmission mode.

A technique was used that provided two-dimensional mapping of diffraction patterns (2θ scans at different azimuthal angles, ϕ) while maintaining the θ–2θ coupling (Bragg condition). Nineteen X-ray spectra were acquired, one for each 5° increment in ϕ, from 0 to 90°. Since the fiber is cylindrically symmetric, only one quadrant of the diffraction pattern was needed.

The degree of crystallinity, $\%n$, was calculated by deconvoluting the pattern resulting from the summation of the nineteen cosine ϕ weighted ($\theta - 2\theta$) diffraction curves. The degree of crystallinity is the ratio of the crystalline area in the region of 5 to 35° (2θ) to the total area. The crystallite dimensions, τ and size, were determined from the peak widths using the Scherrer equation and corrected for instrumental broadening. The crystal orientation functions, f_c, were calculated from the azimuthal scan at fixed 2θ Bragg angle.

The total amorphous component was calculated from difference ($100 - \%n$). The amorphous component was separated into OA and UOA fractions from the two-dimensional diffraction pattern at different ϕ, according to methodology developed by Jellinek and colleagues.[15] The amount and orientation function of the OA component was extracted and calculated as follows. The amorphous curve was first deconvoluted for each spectrum with a simple profile centered at about 18–22° (2θ). The amorphous intensity profile was determined by plotting the amorphous peak height versus ϕ. The amorphous orientation was calculated from the full width at half maximum from this curve. The changing component of the amorphous intensity is the OA component while the unchanging component is the UOA component. The ratio of OA component to the total amorphous component was then extracted from the ratio of their areas.[35]

SAXS

Small-angle X-ray scattering (SAXS) measurements were carried out using a Rigaku pinhole small angle apparatus mounted on a high intensity rotating anode generator. A two-dimensional charge coupled device (CCD) detector and filtered copper K_α radiation were employed. The long period distance, lpd, was calculated from the 4-point pattern in the SAXS image.

RESULTS AND DISCUSSION

Microscopy

OM, SEM, and TEM micrographs of fibers are presented in Figures 3–7. A composite of OM micrographs of longitudinal fiber sections from each stage in the fiber treatment is shown in Figure 3.

The as-spun yarns S1, S1a, S2, S3 and the multistage hot drawn yarns D1, D2, D3 appear bright in polarized light micrographs (S1, S2, D2 are not shown) and featureless except for interference bands that run parallel to the fiber axis. The latter results from the thickness change from fiber edge to center and is seen in all fibers.

An s/fc microstructure can be seen in the images of the cold drawn yarns II, III, IV, and V indicating that the microstructure is present at each step in the conversion from II to IV and from II to V.

The fibrils in the core of s/fc fibers were visible at 1000× magnification as dark features at every angle of the fiber to the polarizers. This indicates that the core is not highly birefringent or highly oriented. In contrast, the sheath was bright when the fiber was oriented at a 45° angle to the polarizers but became dark when oriented parallel to either polarizer. This indicates the polymer in the sheath is highly oriented along the fiber axis. In addition, the core appears more opaque than the sheath in bright field optical microscopy. This observation suggests that the core structures cause more light scattering than the sheath.

An s/fc microstructure in the cold drawn yarn II is also evident in the angled cross section in Figure 4. The core is filled with a multitude of dark continuous streaks extending along the fiber axis. The streaks are regions that differ slightly in birefringence from the surrounding matrix. We attribute these streaks to the fibrillar microstructure in the core of the fiber. The streaks have a diameter of approximately 0.1 μm.

Slit-like voids can be seen in the SEM micrograph of the fibrillar core of the cold drawn yarn II in Figure 5. The slits were not present in the spun yarn S1a before cold drawing or in the multistep hot drawn yarns D1, D2 and D3. Slits are present in cores of each of the cold drawn yarns II, III, IV, and V. The slits are present in the core between fibrils but not present in the sheath. The slit voids appear to be formed at the instant that the fibrils are formed and simultaneously pulled apart by the extreme stress of cold drawing. In II, the slit voids have typical width and length dimensions of

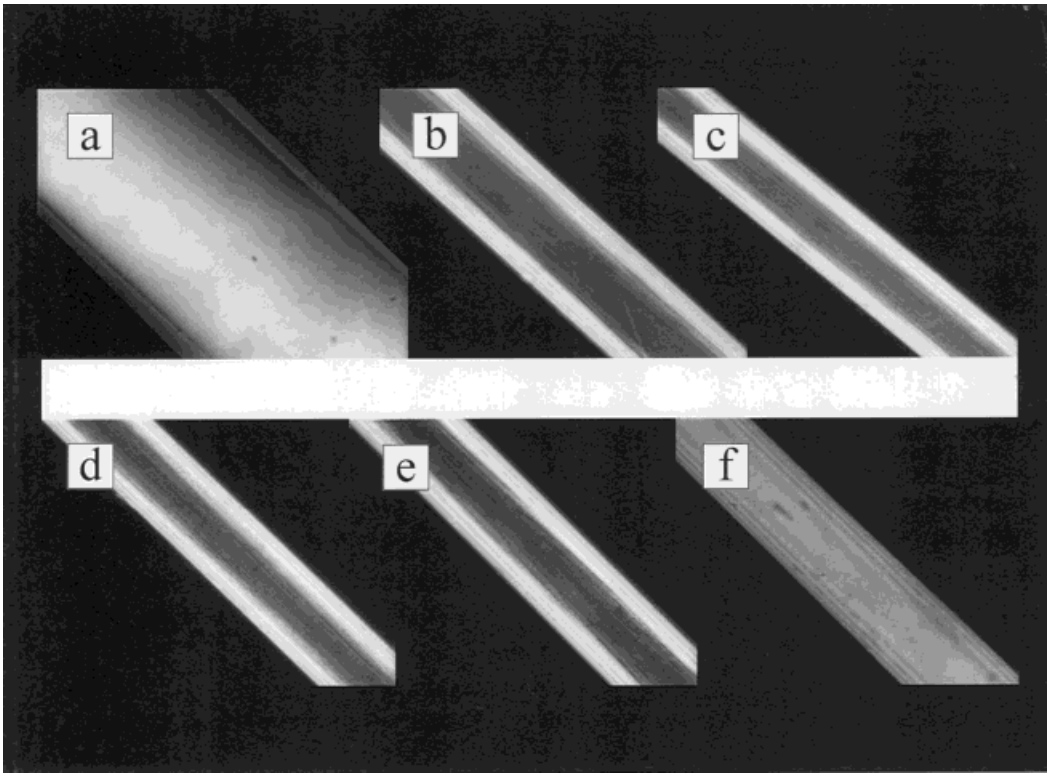

Figure 3 Polarized-light micrographs of fibers at various stages of processing: a) S1a, b) II, c) III, d) IV, e) V, f) D1. Original images at 1000× magnification.

0.4 × 5 μm and are aligned with the fiber axis. The size and number of voids are greatest in II, which also exhibits the lowest density (Table II). There are fewer, smaller slits in III, and IV after annealing, and the densities of these fibers are higher. The magnitude of the density difference between slit-free spun yarn and the somewhat crystalline, voidy drawn yarn is 0.03 g/cc. This suggests that the slit void volume as a percent of the total fiber volume is about 1 to 2%.

The s/fc microstructure of II is also evident in the TEM micrograph of fiber cross-sections in Figures 6 and 7. The core with a diameter of approx-

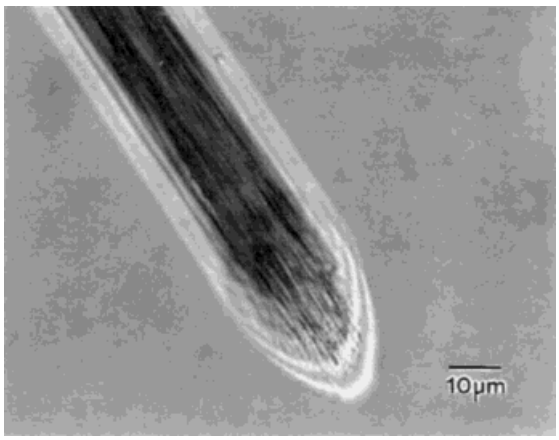

Figure 4 Polarized light optical micrograph of fiber II. Fiber end cut at an angle to show fibril ends in the core.

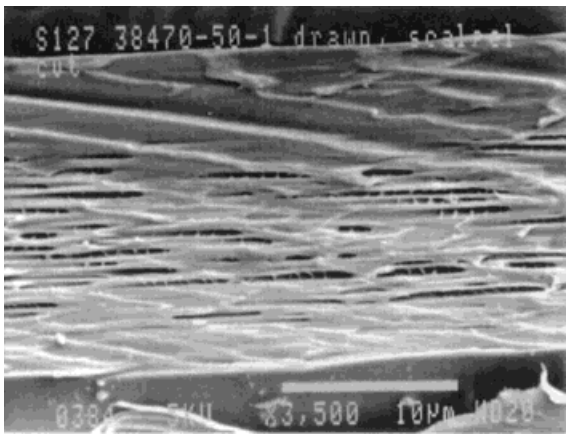

Figure 5 SEM of a longitudinal section of II. The sheath has been peeled back to expose the interior.

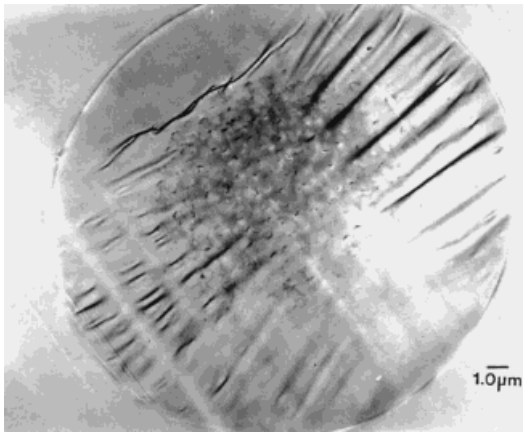

Figure 6 TEM of a cross-section of II.

imately 23 μm occupies about 73% of the area of the cross-section of the 27-μm-diameter fiber. The sheath is a smooth featureless region. The core appears to be composed of microfibrils approximately 0.1 μm in diameter. As shown in Figures 6 and 7, some artifacts (smearing and distortion) are introduced during microtomy because of the extremely tough nature of the fibrillar core. No voids are apparent in the transverse cross section in the TEM image in Figure 6, but a few voids can be seen the longitudinal cross section in the TEM image in Figure 7.

The core region appears much darker than the sheath region in Figure 7. This type of contrast can be caused by a difference in either electron density or diffraction power of the material. Since the core is not much denser than the sheath as suggested by the contrast in the transverse cross sectional view (Fig. 6), the high contrast shown in Figure 7 is likely to be caused by the higher crystallinity in the core.

Attempts were made to measure the birefringence of fibers having an s/fc microstructure. This failed because the interference bands could not be followed across the dark core of a fiber.

WAXS and SAXS

Wide- and small-angle X-ray spectra and data are presented in Figure 8 and Table IV.

The WAXS spectrum of the 200 mpm yarn S1a [Fig. 8(Aa)] has only a strong broad peak and a much smaller second-order peak, indicating that the fiber is amorphous. The band height is relatively unchanging with ϕ (unsloped), indicating that the amorphous component is essentially UOA. The SAXS spectrum of S1a [Fig. 8(Ba)] has a very small "central spot" with a slight horizontal extension ("horizontal streak"), indicative of angstrom-size void scattering.

The WAXS spectrum of the 2000-mpm yarn S2 (not shown) has broad peaks similar to S1a however, more steeply sloped indicating a higher OA content (26.6%) in S2 due to the increased extrusion rate. The SAXS spectrum of S2 (not shown) is similar to S1a.

The WAXS spectrum of the 4000-mpm yarn S3 [Fig. 8(Ab)] has resolved peaks attributable to PET crystallites overlying a much reduced broad peak from the amorphous component. The degree of crystallinity is 26.9%. The SAXS spectrum of S3 [Fig. 8(Bb)] is similar to that of S2 but has an X pattern close to the origin. The X pattern probably arises from deformed "row" crystals. These are crystallites arranged in bands projecting from the fiber surface to the core. The bands are deformed in the sense that the bands are tilted from a perpendicular to the fiber axis. It appears that the crystallites are more concentrated in the bands at the fiber surface than at the core.[36]

Each of the hot drawn yarns D1, D2, and D3 has a highly oriented, semicrystalline microstructure and similar WAXS spectra [D1, Fig. 8(Ac); D2, not shown; D3, Fig. 8(Ad)]. The SAXS spectra have classic 2- or 4-point patterns [D1, Fig. 8(Bc); D2, not shown; D3, Fig. 8(Bd)]. The latter are attributed to crystallites that are arrayed in checker board pattern.[37] The WAXS spectrum of II [Fig. 8(Ae)] has somewhat poorly resolved peaks attributable to small crystallites and a reduced amorphous background compared to S1a [Fig. 8(Aa)]. A degree of crystallinity of 20.1% with a measurable crystallite size (67 nm[3]) is present in II. However, this crystallinity is less in

Figure 7 TEM of a low-angle cross-section of II.

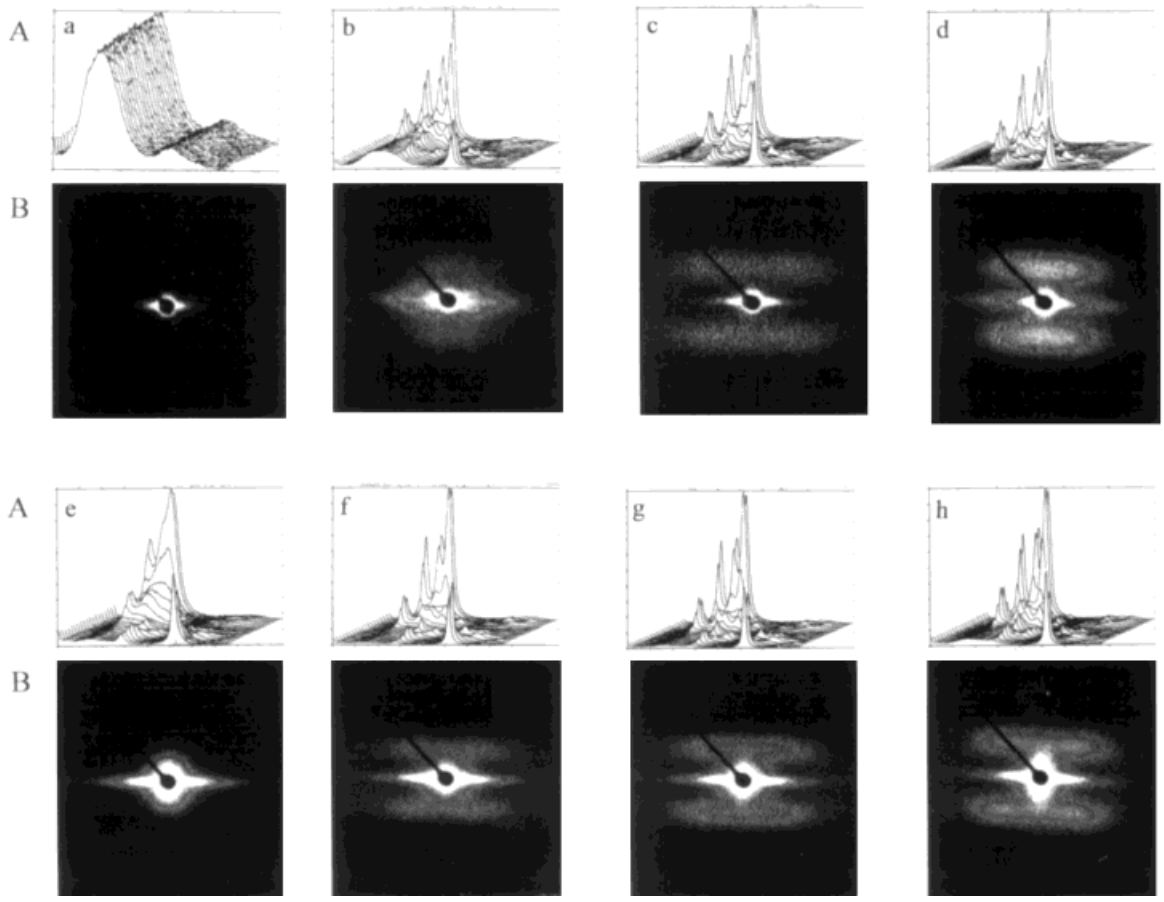

Figure 8 A. Wide-angle X-ray spectra. B. Small-angle X-ray spectra. (a) S1a, (b) S3, (c) D1, (d) D3, (e) II, (f) III, (g) IV, and (h) V.

degree and the crystallites smaller in size than that present in D1, D2, and D3. The amorphous component in II has a large OA content (74.7%), the highest OA content in any yarn in Table IV. The crystalline and amorphous components are moderately oriented with the fiber axis ($f_{c_{\bar{1}05}} = 0.946$ and $f_a = 0.807$, respectively).

The SAXS pattern of II [Fig. 8(Be)] has a different appearance than SAXS patterns for other semicrystalline yarns; specifically, the spun yarn S3 and the hot drawn yarns D1, D2, and D3. II exhibits a large central spot with no X pattern and a significant horizontal steak. There is no meridional scattering; that is, no 2- or 4-point pattern. We believe that the crystallites seen here in II may be localized in the fibrils in the core and that the OA component arises from extended polymer chains in both the sheath and the matrix around fibrils in the core. In contrast to high speed yarns, the concentration of crystallites in II is surface poor and core rich.

The horizontal streak is attributed to microvoid scattering. The microvoids are thought to have dimensions in the 50–500 Å range. These are in addition to the larger slit-like voids seen by SEM (seen earlier).

The WAXS spectrum of III [Fig. 8(Af)] has highly resolved peaks attributable to PET crystallites. Annealing under tension caused an increase in crystalline perfection with increases in both the degree of crystallinity (46.1%) and crystallite size (to 123 nm^3). The OA component is sharply lower in III (50.3%, down from 74.7% in II) yet the UOA component remains low (3.6%). This indicates that the crystal growth occurred at the expense of the OA component. These new crystallites add to the already present crystallites in the fibrils of II. The crystalline and amorphous components are highly oriented ($f_{c_{\bar{1}05}}$ and f_a are 0.976 and 0.845, respectively). The SAXS spectrum [Fig. 8(Bf)] for the annealed yarn III has a large central spot, a horizontal streak, and the

Table IV Wide and Small Angle X-Ray Diffraction Data

	S1a	S2	S3	II	III	IV	V	D1	D2	D3
WAXS										
τ_{010} Å	[b]	[b]	63	40	63	70	70	62	61	70
τ_{100} Å	[b]	[b]	54	39	46	49	50	47	46	52
τ_{105} Å	[b]	[b]	52	43	42	44	46	41	40	48
$\tau_{1\bar{1}0}$ Å	[b]	[b]	60	28	74	75	67	69	67	69
size[a], nm^3	[b]	[b]	174	67	123	151	161	119	112	172
fc 010	0	0	0.963	0.959	0.972	0.969	0.957	0.963	0.970	0.971
fc 100	0	0	0.975	0.972	0.979	0.976	0.971	0.975	0.978	0.979
fc $\bar{1}05$	0	0	0.967	0.946	0.976	0.973	0.954	0.971	0.977	0.977
fc $1\bar{1}0$	0	0	0.978	0.976	0.987	0.986	0.979	0.986	0.988	0.987
diff. $\bar{1}05$	0	0	18.28	16.62	20.1	18.69	16.32	17.02	19.67	19.91
fa	0	0.545	0.788	0.807	0.845	0.856	0.800	0.824	0.858	0.832
%n	0	0	26.9	20.1	46.1	50.6	49.6	45.2	37.9	41.7
by WAXS										
OA, %	9	26.6	17.7	74.7	50.3	39.9	30.1	44.4	47.7	39.1
UOA, %	90	73.4	55.5	5.2	3.6	9.5	20.3	10.4	14.4	19.2
SAXS										
SAXS lpd,[c] Å	—	—	—	—	123	122	113	104	102	119
SAXS pattern	small central spot	small central spot	small central spot	large central spot	large central spot	large central spot	large elliptical central spot	small central spot	small central spot	small central spot
				horizontal streak	horizontal streak	horizontal streak	horizontal streak			
			X pattern near origin		faint 4-pt. pattern	4-pt. pattern	intense 4-pt. pattern	faint 4-pt. pattern	4-pt. pattern	intense 2-pt. pattern
Crystallite morphology	amorphous	amorphous	semicrystalline	randomly arrayed crystallinity microvoids	checker-board array microvoids	checker-board array microvoids	checker-board array microvoids	checker-board array		deformed row crystallinity

[a] Size: $\tau_{010} \times \tau_{100} \times \tau_{105}$.
[b] Too low to measure.
[c] lpd, long period distance.

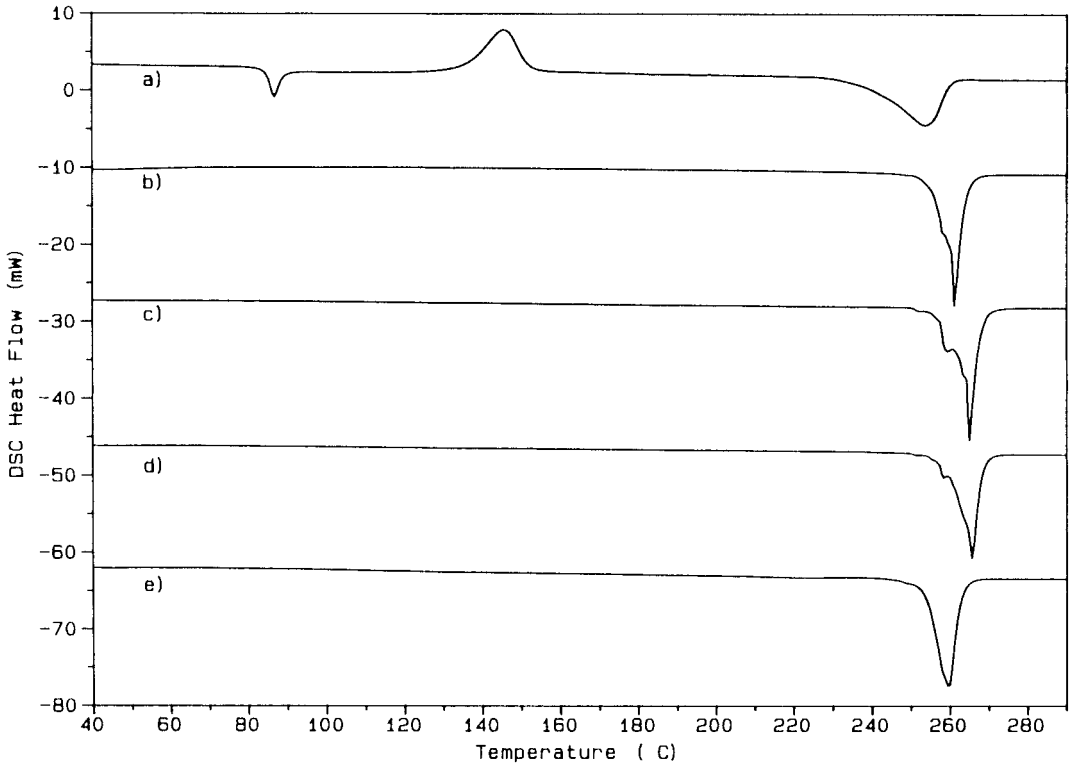

Figure 9 Taut fiber DSC thermograms, 40–290°C: (a) S1a, (b) II, (c) III, (d) IV, and (e) V.

beginning of the classic 4-point pattern with an lpd of 123 Å.

Qualitatively, the WAXS and SAXS spectra of IV [Fig. 8(Ag) and 8(Bg)] are similar to III. Both exhibit emerging SAXS 4-point patterns indicating that there is no major change in the macro arrangement of the crystallites.

The WAXS spectrum of V [Fig. 8(Ah)] is similar to that of the annealed and relaxed yarns III and IV [Fig. 8(Af) and 8(Ag)]. The SAXS spectrum of V [Fig. 8(Bh)] has a well-developed 4-point pattern with a large elliptical central spot and a prominent horizontal streak.

Thermal Properties

Taut DSC scans of yarns S1a, II, III, IV, and V are presented in Figures 9 and 10. The properties of these and the reference yarns S2, S3, D1, D2, and D3 are tabulated in Table V.

The taut DSC scans of each of the spun yarns exhibits a glass transition T_g and a cold crystallization exotherm T_{cc} indicative of the presence of an amorphous component and a melting endotherm in the range 253.8–268.4°C indicative of crystalline components. In addition, S1a has an endotherm due to aging overlying the T_g. By DSC, S1a has a low degree of crystallinity (8%) while the higher speed yarns S2 and S3 exhibit higher degrees of crystallinity (16.6 and 34.7%, respectively). This compares with 0, 0, and 26.9% crystallinities by WAXS, respectively.

The taut DSC heating scans of II, III, IV, and V have only one feature, a composite of crystallite melting endotherms at temperatures, T_m, in the 248.8–265.6°C range. Absent are T_g and T_{cc} indications of an amorphous component.

It has been observed in our experience[38] that the amorphous components in taut DSC scans of drawn PET fibers do not exhibit the glass or cold crystallization transitions at the usual T_g or T_{cc} where they appear in the taut DSC of as-spun yarns. This seems related to the character of the amorphous content in the drawn yarns—which is predominantly OA—and is particularly striking in the case of II, which has a particularly high amorphous content (74.7% OA by WAXS). III, IV, and V also have substantial OA contents (30.1–50.3% by WAXS). The spun yarns have low OA contents (9–26.6%) and high UOA (90–55.5%) contents. It appears that the taut DSC scan is

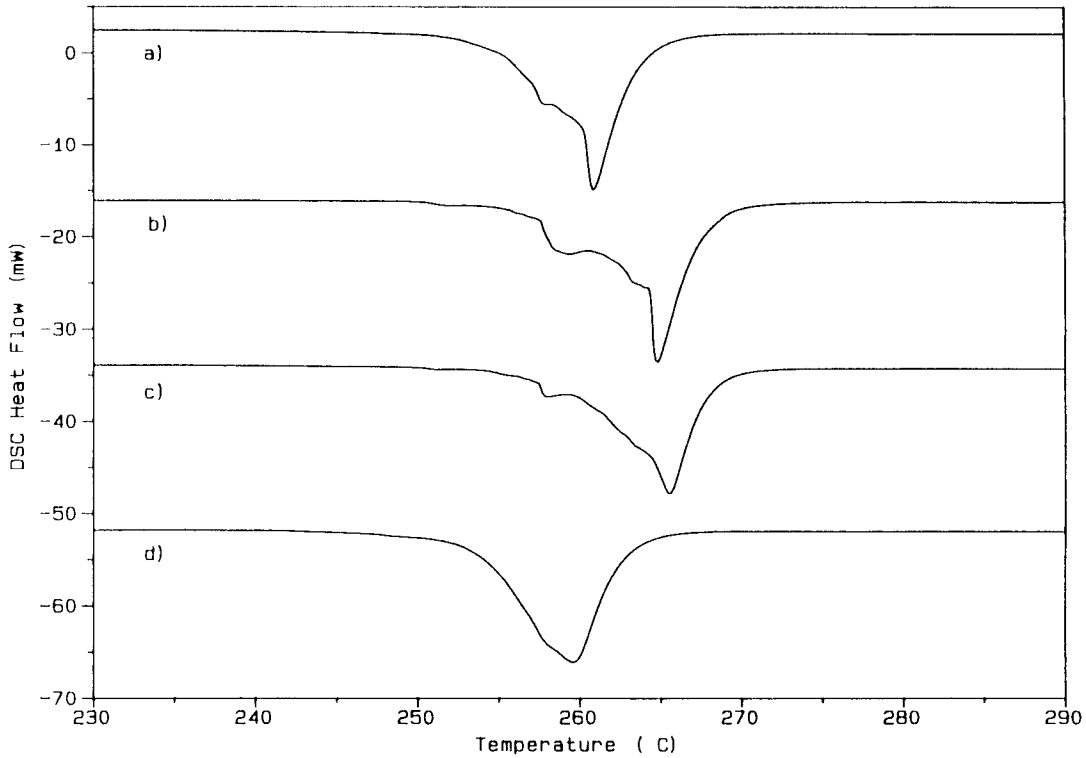

Figure 10 Taut fiber DSC thermograms—melting endotherm region, 230–290°C: (a) II, (b) III, (c) IV, and (d) V.

insensitive to the OA component in drawn yarns. The lack of sensitivity might be due to (1) the restricted mobility imposed by the taut condition, (2) a small free energy difference between the OA component and its crystalline counterpart, and (3) the possibility that the T_g and T_{cc} transitions are spread over a wide temperature range. We assume that during the DSC scan of drawn yarns, the OA component does not attain adequate mobility to exhibit a glass transition or to crystallize until temperatures near T_m are reached. As T_m is approached, the OA content gains mobility and crystallizes. T_g and T_{cc} are obscured by the more intense composite T_m. The newly formed crystallites quickly melt when their T_m is reached.

The crystalline contents of yarns with a s/fc microstructure—as determined by taut DSC scans and by WAXS—are compared in Table VI. For the crystallinity of II, the two techniques diverge. For the reason cited earlier we assume that WAXS portrays the state of II more accurately than DSC. Some of the OA component in II crystallized during the DSC scan leading to the high degree of crystallinity observed by DSC.

II, III, IV, and V each exhibits a melt endotherm shoulder in the 257.9–259.4°C range and other main melt endotherms. Since a fibrillar core is the common component in these samples, we attribute these shoulder endotherms to the melting of crystallites in the fibrils in the core of fibers.

II exhibits a substantial (ΔH_m = 59.5 J/g) melt endotherm consisting of (1) a shoulder at 257.9°C due to the melting of crystallites in the fibril core and (2) a main component at 260.9°C due to the melting of crystallites that formed from the OA component during the DSC scan.

The melt endotherm of III is a composite of three shoulder endotherms and a main endotherm. The total crystallization enthalpy increased to 62.2 J/g reflecting the increased degree of crystallinity in III. The shoulder at 259.4°C is attributed to melting of the crystallites in the fibrils in the core, as before. The shoulders at 252.8 and 263.7°C are attributed to melting of crystallites that formed from the OA component during the DSC scan. The main endotherm in III at 264.8°C—and similar endotherms in IV, D2, and D3 in the high temperature range 263 to 273°C—are attributed to the melting of crystallites that formed from the OA component during annealing under high tension at 200°C.

Table V Thermal Properties of Cold Drawn and Reference Yarns

	T_g (°C)	T_{cc} (°C)	ΔH_{cc} (J/g) − = exo	T_m (°C)	ΔH_m (J/g) + = endo	$\%n$ by DSC (%)
S1a	~ 80	145.6	−30.7	253.8	41.9	8.0[b]
S2	79.9	99.8	−24.0	254.4	47.0	16.6[b]
S3	82.9	107.3	−7.0	268.4	55.6	34.7[b]
II	—	—	—	257.9 s[a]	59.5	42.5[c]
				260.9 m		
III	—	—	—	252.8 s	62.2	44.4[c]
				259.4 s		
				263.7 s		
				264.8 m		
IV	—	—	—	251.0 s	66.1	47.2[c]
				258.0 s		
				263.3 s		
				265.6 m		
V	—	—	—	248.8 s	53.8	38.4[c]
				258 s		
				259.4 m		
D1	—	—	—	245.7 s	59.2	42.3[c]
				256.8 s		
				259.6 m		
D2	—	—	—	268.1 m	59.5	42.5[c]
D3	—	—	—	273.1 m	61.0	43.6[c]

[a] s, shoulder; m, main peak.
[b] Degree of crystallinity (DSC), $\%n = (\Delta H_m - \Delta H_{cc}) \times 100/140$ J/g.
[c] Degree of crystallinity (DSC), $\%n = \Delta H_m \times 100/140$ J/g.

The melt endotherm of V is a broad peak with features at 258° and 259.4°C. There are no endotherms in the high temperature range. The feature at 259.4°C is attributed to the melting of crystallites in fibrils at the core. The feature at 258°C and below is attributed to the melting of crystallites that formed indirectly from the OA component in II when it was relaxed at 200°C under low tension. During this processing the OA content decreased and the UOA content increased dramatically (compared to II). It appears that the OA content first transformed to UOA content in the absence of sufficient tension to maintain orientation; then, the UOA component crystallized forming the crystallites melting at 258°C.

Table VI Comparison of Crystallinities by DSC and WAXS

	% Crystallinity	
	Taut DSC	WAXS
II	42.5	20.1
III	44.4	46.1
IV	47.2	50.6
V	38.4	49.6

Tensile Properties, Shrinkage, and Dimensional Stability

The tensile and shrinkage properties of s/fc yarns and reference yarns are presented in Table VII.

II, III, and IV exhibit somewhat higher strengths and relatively high stiffnesses (initial moduli) for PET yarns. Each has an s/fc microstructure. In addition, the orientation of the amorphous and crystalline phases in these yarns was either generated under high tension (II) or preserved with tension during annealing and relaxing (III and IV). V suffered a loss in tensile properties. This is a yarn whose microstructure and orientation was generated under high tension but then allowed to transform during the relaxation under low tension (although the s/fc structure survived unchanged).

II exhibits highest shrinkage (20.9%) due to its high OA content and low degree of crystallinity. III, IV, and V exhibit lower shrinkages (9.4, 3.3,

Table VII Tensile Properties and Dimensional Stability

	Ten. (g/den)	Elong. (%)	i.Mod. (g/den)	EASL at 2 gpd	HAS at 177°C	Dimensional Stability Index (EASL + HAS)[a]
II	6.8	10.4	141	1.19	20.9	22.1
III	9.8	6.5	173	0.73	9.4	10.1
IV	8.5	13.4	129	1.31	2.0	3.3
V	5.6	38.6	82.6	9.35	1.3	10.7
D1	5.3	14.0	116	2.46	7.4	9.9
D2	8.0	7.7	112	1.94	6.2	8.2
D3	5.1	14.8	106	1.90	4.8	6.7

[a] Lowest value, highest dimensional stability.

and 1.3%, respectively) due to their reduced the OA content and increased the degrees of crystallinity. Surprisingly, the fibrillar core is not effective in restraining this shrinkage.

D1, D2, and D3 exhibit typical properties for hot drawn PET yarns. The hot air shrinkages of D1, D2, and D3 are typical.

The development of yarn dimensional stability as the result of processing (spinning, drawing, annealing, relaxing, or heat treating) is traced in Figure 11 where stiffness (i.e., modulus) is plotted against shrinkage (HAS). The properties of yarns with s/fc microstructure are compared to those of the reference yarns.

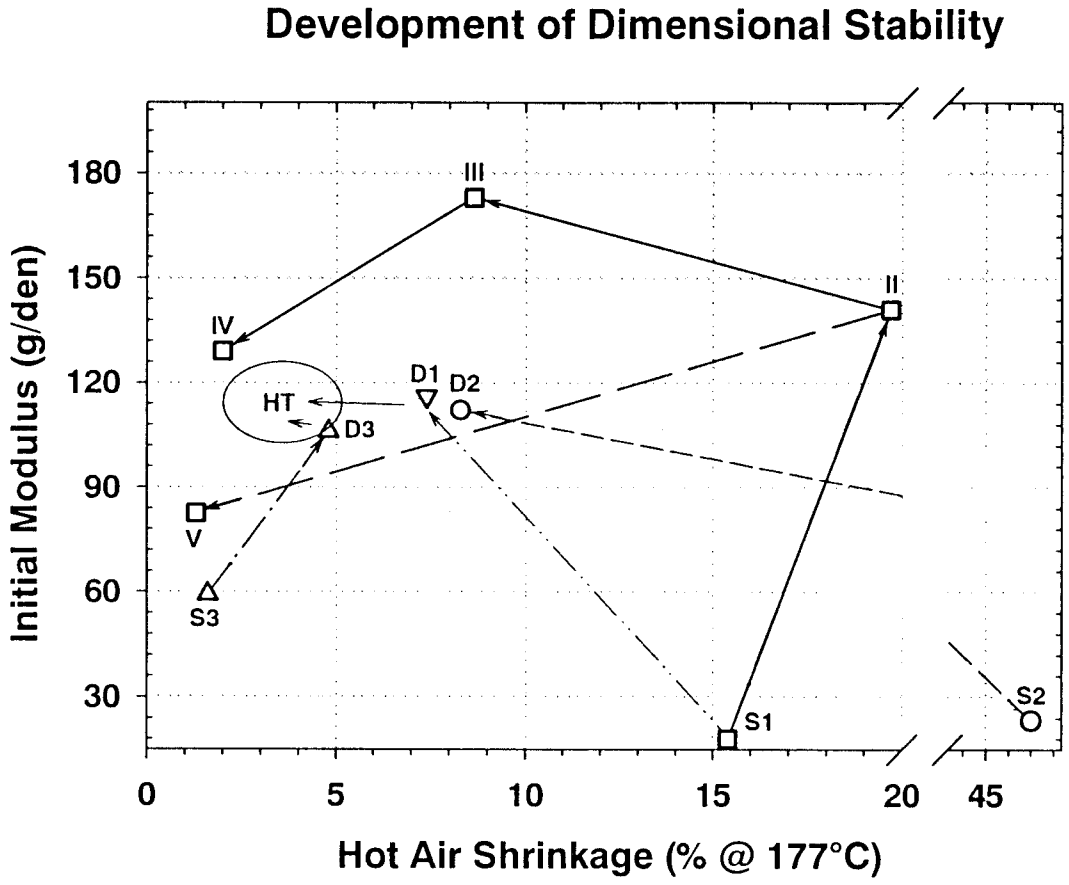

Figure 11 Development of dimensional stability.

The sequences S1 ⇒ D1 ⇒ HT, S2 ⇒ D2 ⇒ HT, and S3 ⇒ D3 ⇒ HT are representative of yarn spinning, hot drawing by conventional multistage techniques, and heat treating under conditions that simulate tire yarn conversion to tire cord. The widely differing moduli and shrinkage properties of S1, S2, and S3 are due to the differing microstructures produced during extrusion. S1 exhibits low modulus and moderate shrinkage because it is unoriented and noncrystalline. S2 shrinks most because it has a degree of polymer chain extension and alignment (OA content) with a low degree of stabilizing crystallinity. S3 exhibits the highest modulus and lowest shrinkage because it has a high degree of chain extension and alignment and also stabilizing crystallinity.

The modulus/shrinkage properties of the multistage hot drawn yarns D1, D2, and D3 are more closely clustered. Their dimensional stability indices range from 6.7 to 9.9. Each has a variant of the microstructure described by the three-phase model.[3]

In processing that mimics the conversion from tire yarn to tire cord, the drawn yarns D1, D2, and D3 were converted to HT yarns. Because the shrinkage of HT yarns is lower, the dimensional stability of the HT yarns is often improved.

The sequence S1a ⇒ II ⇒ III ⇒ IV produces an s/fc yarn that has been exposed to a heat treatment (annealing under tension, relaxing under controlled tension) that is at least as severe as that undergone by the HT yarns. Even so, IV has a more favorable combination of stiffness and shrinkage than any of the HT yarns and exhibits the highest dimensional stability (3.3, lowest index value).

The sequence S1a ⇒ II ⇒ V produces an s/fc yarn that exhibits low modulus, low shrinkage, and low dimensional stability (10.7 index). Relaxing under low tension without annealing (II ⇒ V) converts more of the OA content in II to UOA content and low melting crystallinity in V than does annealing and relaxing under tension (II ⇒ III ⇒ IV). This illustrates the importance of controlling the annealing and relaxation processing to convert the OA component in II to a balance of OA content and highly oriented, high melting crystallite arrays, as in IV.

SUMMARY

Spun Yarns

S1 is a yarn that was formed at a low spin speed (extrusion rate) and is unoriented, noncrystalline as a result. S1a was formed from S1 by sub-T_g aging. An s/fc microstructure could be generated in S1a, but not routinely in S1, by cold drawing to high draw ratios. S2 and S3 are yarns that were formed at higher spin speeds and have a degree of orientation or degree of both orientation and crystallinity as a result. Neither S2 or S3 could be cold drawn to high draw ratios and, even though a cold neck formed in each case, neither yielded an s/fc microstructure. We believe that the greater orientation present in these high speed yarns is an obstacle to the formation of the s/fc microstructure on cold drawing.

Cold Drawn Yarn II

S1a was cold drawn in one step with near-breaking line tensions such that a cold neck formed and a high draw ratio (6 : 1) resulted yielding II. II has an s/fc microstructure (optical microscopy), a low density (>1.310 g/cc) due to slitlike voids (SEM, TEM), and a degree of crystallinity (20.1% by WAXS). The crystallites are not well organized (no SAXS pattern) and melt in a range (257.9–259.4°C) associated with the melting of crystallites in the fibrils in the core. II has a very high OA content (74.7%) attributable to extended and aligned polymer chains in the sheath and matrix surrounding the fibrils.

The high OA content contributes to the high stiffness and shrinkage of II. Unfortunately, the fibrillar core does not act to restrain this shrinkage. II exhibits poor dimensional stability.

Annealed Yarn III

II was annealed under high tension yielding III. The s/fc microstructure survived this processing. The fibrillar core in III is similar to that in II, except that the voids are reduced in size and number. As with II, there is an endotherm attributable to the melting of crystallites in the fibrillar core. III has lower OA and UOA contents (50.3% and 3.6%, respectively) and a substantially higher degree of crystallinity (46.1%). As the result of annealing under tension, the OA content in II appears to have been directly converted to additional new crystallites in III without allowing an increase in UOA content. These additional crystallites melt (264.8°C) in a higher temperature range (263–266°C), a characteristic of crystallites that were formed directly from an OA component under high tension. It is suggested that these high T_m crystallites may be formed from extended chains as opposed to folded chains.

III exhibits the highest tensile strength and highest stiffness, but it still exhibits a relatively high shrinkage. We attribute the stiffness of III to the remaining OA content, the increased degree of crystallinity, the presence of high T_m crystallites, and the s/fc microstructure. The increased degree of crystallinity and reduced OA content combine to reduce shrinkage from that in II. While improved, the dimensional stability of III (10.1 index) is still poor.

Annealed and Relaxed Yarn IV

III was briefly treated at lower line tension to generate IV in order to allow some of the OA content in III to relax and thereby reduce shrinkage. A fibrillar core is still present in IV. The slitlike voids are reduced in number and size in IV and the density increased to 1.355 g/cc. Relaxing produced a lower OA content in IV (39.9%), a higher UOA content (9.5%), and a higher degree of crystallinity (50.6%). As in II and III, a crystallite melting at 258°C characteristic of the fibrillar core was present. IV has crystallites melting in the high temperature range. In addition, a low T_m crystallite was generated in IV. This crystallite apparently formed when some OA $\Rightarrow$ UOA conversion occurred and the later crystallized yielding crystallites that melt at 251°C. It is suggested that these crystallites are not as perfectly formed as the high T_m crystallites. Perhaps they are formed from polymer chains that include occasional folds.

IV exhibits lower stiffness and a much lower shrinkage (2.0%); both are attributable to the lower OA content. However, a better balance between stiffness and shrinkage was achieved with the result that IV is the most dimensionally stable yarn (3.3 index) studied here. The properties of IV can properly be compared to those of the HT yarns. Like the HT yarns, IV has undergone processing (annealing and relaxing) that is similar in severity (temperature, line tension, and residence time) to that encountered during the conversion of tire yarn to tire cord and subsequent tire building.

Relaxed Without Annealing Yarn V

II was relaxed at low tension without annealing, yielding V. Remarkably, the s/fc microstructure is still present in V and crystallites melting in the range 257.9–259.4°C associated with the fibrillar core are present. Relaxing without annealing produced a sharply reduced OA content (39.9%) and a sharply increased UOA content in V. The OA content in II appears to have been converted to new UOA content and new crystallites in V. The new crystallites in V melt in the low and middle T_m ranges. There are no crystallites present that melt in the high T_m range. This suggests that the new crystallites formed indirectly from the OA component in II via the UOA component.

V exhibits lower shrinkage but much lower stiffness with a resultant poor dimensional stability (10.7 index).

Multistage, Hot Drawn Yarns D1, D2, D3

Hot drawing S1, S2, and S3 generated D1, D2, and D3. None of these hot drawn yarns or their heat treated progeny yarns HT exhibits an s/fc microstructure. The microstructure in hot drawn yarns is developed gradually in a multistage process. By contrast, the s/fc microstructure that develops in cold drawn yarns is generated instantaneously in one stage.

CONCLUSIONS

New cold draw processing of aged, unoriented, noncrystalline PET yarn was found that generates a s/fc microstructure in each fiber of the yarn. Cold drawn yarn with this microstructure has a very high OA content (74.7%) and a moderate degree (20%) of crystallinity. The cold drawn fiber density is below that expected for PET and elongated slit-like voids are observed in the core.

The cold drawn yarn can be annealed under tension and relaxed to generate yarn with a dramatically improved dimensional stability. The s/fc microstructure survives all annealing and relaxing processing. The OA content in a cold drawn yarn is converted, directly without the participation of the UOA component, to high T_m crystallites in yarns that have been annealed under high tension. In cold drawn yarns that have been relaxed under low tension, the OA content is converted to UOA content and low T_m crystallites.

The assistance of J. Dibiase (fiber spinning), D. Brikowski (tensile measurements), C. Steele (optical microscopy and TEM sample preparation), T. Aversa (SAXS and WAXS), C. Driscoll (fiber densities), D. Karim, and J. Menczel for helpful discussions are gratefully acknowledged.

REFERENCES

1. Davis, H. L.; Jaffe, M. L.; LaNieve III, H. L.; Powers, E. J. US Pat. 4,101,525 (1978).
2. Davis, H. L.; Jaffe, M. L.; LaNieve III, H. L.; Powers, E. J. US Pat. 4,195,052 (1980).
3. Prevorsek, D. C.; Tirpak, G. A.; Harget, P. J.; Reimschuessel, A. C. J Mater Sci—Phys 1974, B9, 733–759.
4. Prevorsek, D. C.; Kwon, Y. D.; Sharma, R. K. J Mater Sci 1977, 12, 2310–2328.
5. Prevorsek, D. C. In Polymer Liquid Crystals; Ciferri, A.; Krigbaum, W. R.; Meyer, R. B., Eds.; Academic: New York, 1982.
6. Kunugi, T. In Oriented Polymer Materials; Fakirov, S., Ed.; Huthig Verlag, 1996.
7. Kunugi, T.; Suzuki, A.; Hashimoto, M. J Appl Polym Sci 1981, 26, 213–221.
8. Kunugi, T.; Suzuki, A.; Hashimoto, M. J Appl Polym Sci 1981, 26, 1951–1960.
9. Kunugi, T.; Ichinose, C.; Suzuki, A. J Appl Polym Sci 1986, 31, 429–439.
10. Kunugi, T.; Suzuki, A.; Tsuiki, T. Kobunshi Ronbunshu 1991, 48, 703–710.
11. Kunugi, T.; Suzuki, A. J Appl Polym Sci 1996, 62, 713–719.
12. Suzuki, A.; Kobayashi, K.; Kunugi, T. Kobunshi Ronbunshu 1994, 51, 5–10.
13. Suzuki, A.; Kobayashi, K. Kobunshi Ronbunshu 1996, 53, 710–715.
14. Suzuki, A.; Sato, Y.; Kunugi, T. Kobunshi Ronbunshu 1997, 54, 102–107.
15. Suzuki, A.; Sato, Y.; Kunugi, T. J Polym Sci: Part B, Polymer Physics 1998, 36, 473–481.
16. Chen, J.-Y.; Tucker, P. A.; Cuculo, J. A. J Appl Polym Sci 1997, 66, 2441–2455.
17. Marshall, I.; Thompson, A. B. Proc Roy Soc 1954, 541–557.
18. Allison, S. W.; Pinnock, P. R.; Ward, I. M. Polymer 1966, 7, 66–69.
19. Allison, S. W.; Ward, I. M. Br J Appl Phys 1967, 18, 1151–1164.
20. Kassenbeck, P. C R Acad Sci 1953, 236, 369.
21. Cobbold, A.; Daubeny, R. D. P.; Deutsch, K.; Markey, P. Nature 1953, 172, 806.
22. Yeh, G. S. Y.; Geil, P. H. J Macromol Sci—Phys 1967, B1, 235–249.
23. Lee, S.; Miyaji, H.; Geil, P. H. J Macromol Sci—Phys 1983, B22, 489–496.
24. Yeh, G. S. Y.; Geil, P. H. J Macromol Sci—Phys 1967, B1, 251–277.
25. Wolpert, S. M.; Weitz, A.; Wunderlich, B. J Polym Sci: A-2 1971, 9, 1887–1905.
26. Menczel, J.; Wunderlich, B. J Polym Sci: Polym Let Ed 1981, 19, 261–264.
27. Montserrat, S.; Cortes, P. Makromol Chem Macromol Symp 1988, 20/21, 389–395.
28. Montserrat, S.; Cortes, P. J Mater Sci 1995, 30, 1790–1793.
29. Wang, Y.; Shen, D. Polym J 1997, 29, 860–863.
30. Qian, R.; He, J.; Shen, D. Polym J 1987, 19, 461–466.
31. Qian, R.; et al. Macromol 1993, 26, 2950–2953.
32. Qian, R.; Shen, D.; Wu, L. Macromol Chem Phys 1996, 197, 1485–1493.
33. Jaffe, M.; Menczel, J. D.; Bessey, W. E. In Thermal Characterization of Polymeric Materials; Turi, E. A., Ed.; Academic: New York, 1981.
34. Wunderlich, B. In Macromolecular Physics; Academic: New York, 1980.
35. Jellinek, G.; Ringens, W.; Heidemann, G. Ber Bunsenges Phys Chem 1970, 74, 924–929.
36. Saw, C., unpublished results, 1998.
37. Rao, B. R.; Datye, K. V. Syn Fibres 1996, Jul/Sep, 15–25.
38. Menczel, J. A., unpublished results, 1997.